ACCSCIENCE PUBLISHING

International Journal of Bioprinting

RESEARCH ARTICLE

# Enhancing osteogenesis using 3D-printed porous tantalum scaffolds: A biomechanical, *in vivo*, and *in vitro* study

**Mengxiao Tantai[1,2,3†], Yi Zhang[1,2,3†], Chengbin Wang[2,3], Tongwei Du[4], Sihao Yu[1,2,3], Zhihai Zhang[1,2,3], Hui Ma[3], Junliang Song[3], Dong Qu[5], Gangning Feng[1,2,3*], and Zhidong Lu[1,2,3*]**

[1]Department of Spinal Surgery, General Hospital of Ningxia Medical University, Yinchuan, Ningxia, China

[2]Institute of Osteoarthropathy, Institute of Medical Sciences, General Hospital of Ningxia Medical University, Yinchuan, Ningxia, China

[3]The First Clinical Medical School, Ningxia Medical University, Yinchuan, Ningxia, China

[4]State Key Laboratory for Manufacturing System Engineering, School of Mechanical Engineering, Xi'an Jiaotong University, Xi'an, Shaanxi, China

[5]School of Metallurgical Engineering, Xi'an University of Architecture and Technology, Xi'an, Shaanxi, China

[†]These authors contributed equally to this work.

***Corresponding authors:**
Zhidong Lu
(15709600520@163.com)

Gangning Feng
(2867734776@qq.com)

**Citation:** Tantai M, Zhang Y, Wang C, *et al.* Enhancing osteogenesis using 3D-printed porous tantalum scaffolds: A biomechanical, *in vivo*, and *in vitro* study. *Int J Bioprint.* 2025;11(6):499-514. doi: 10.36922/IJB025390395

**Received:** September 23, 2025
**Revised:** October 4, 2024
**Accepted:** October 11, 2025
**Published online:** October 14, 2025

**Copyright:** © 2025 Author(s). This is an Open Access article distributed under the terms of the Creative Commons Attribution License, permitting distribution, and reproduction in any medium, provided the original work is properly cited.

**Publisher's Note:** AccScience Publishing remains neutral with regard to jurisdictional claims in published maps and institutional affiliations.

## Abstract

Complex bone defects continue to pose significant challenges in the field of orthopedics, where restoring structural integrity and promoting osteointegration are essential for successful repair outcomes. Three-dimensional (3D) printing offers a robust approach for fabricating patient-specific scaffolds with precise architectural and functional control. In this study, we designed and fabricated porous scaffolds composed of tantalum and titanium alloys, both with identical porosity, utilizing 3D printing technology. We systematically compared their mechanical properties, *in vitro* osteogenic potential, and *in vivo* bone integration within a defect model. The porous tantalum (PTa) scaffolds demonstrated exceptional biocompatibility, enhanced cell adhesion, and significantly promoted the osteogenic differentiation of mesenchymal stem cells, as well as extracellular matrix mineralization. *In vivo*, the PTa scaffolds not only expedited bone repair but also improved osteoconductive ingrowth compared to their titanium counterparts. Multi-omics analyses further elucidated potential biological mechanisms underlying the superior performance of PTa. These findings underscore the potential of 3D-printed PTa as a promising scaffold material for the clinical repair of bone defects.

***Keywords:*** Biomaterials; Bone regeneration; Multi-omics analysis; Osteogenic differentiation; Porous tantalum

## 1. Introduction

Bone defects currently represent a prevalent clinical challenge in orthopedic practice. Critical-sized bone defects, resulting from trauma, infection, or bone tumors, frequently

exceed the regenerative capacity of autologous bone grafts, making repair difficult. These defects have emerged as a significant global health concern, adversely impacting patients' quality of life. As a result, biomaterials research has focused on developing innovative bone substitutes.[1] Traditionally, autologous bone grafting has been considered the "gold standard" for bone regeneration. Nevertheless, its clinical utility is constrained by the limited availability of donor tissue and the invasive nature of harvesting.[2]

In recent years, metal-based implant materials have become a key focus due to their potential in bone defect repair. With excellent mechanical performance and favorable biological properties, these materials have been widely applied in the biomedical field. Among them, tantalum, titanium, and their alloys are commonly used in clinical orthopedic practice due to their superior strength and biocompatibility.[3] However, titanium alloys exhibit relatively low bioactivity and limited osteoconductivity. Their high elastic modulus may also lead to stress shielding and localized stress concentration, increasing the risk of implant loosening, fracture, and periprosthetic bone loss.[4]

Tantalum has emerged as a promising alternative due to its remarkable properties. It is characterized by exceptional corrosion resistance and superior biocompatibility, rendering it highly suitable for implant applications.[5] Porous tantalum (PTa), an innovative biomaterial, has shown considerable promise in bone tissue engineering. Its high porosity and interconnected pore structure not only enhance mechanical adaptability but also facilitate osseointegration, promoting new bone formation and long-term implant stability.[6] Furthermore, its low elastic modulus and high surface friction coefficient contribute to the effective reduction of stress shielding, minimization of marginal bone loss, and improvement of initial implant stability.[7]

PTa has been increasingly applied in orthopedic procedures such as hip and knee joint reconstruction,[8] and has also demonstrated encouraging outcomes in dental implants.[9] Compared with conventional titanium, PTa significantly promotes the proliferation and differentiation of primary osteoblasts, particularly in elderly patients, thereby supporting more stable bone integration.[10]

Despite these advancements, the molecular mechanisms by which PTa promotes bone regeneration remain insufficiently understood, with few studies employing multi-omics approaches. To our knowledge, this is the first study to systematically integrate transcriptomic and proteomic analyses to investigate these mechanisms. Structurally identical PTa and porous titanium alloy (PTi6Al4V) scaffolds were fabricated using a uniform process and characterized mechanically. *In vitro*, we compared rabbit bone marrow-derived mesenchymal stem cell (BMSC) adhesion, proliferation, and osteogenic differentiation on both scaffolds. *In vivo*, we assessed bone ingrowth post-implantation. Multi-omics analysis of peri-implant bone tissue revealed distinct biological pathways associated with each material, offering new insights into the molecular basis of PTa-enhanced osteogenesis.

## 2. Materials and methods

### 2.1. Materials

The porous cylindrical scaffolds, measuring 70 mm × 70 mm, were designed with a porosity of 75% and pore sizes ranging from 300 to 600 μm. These scaffolds were modeled using SolidWorks (Dassault Systèmes, France), employing a diamond lattice unit cell structure to delineate the internal geometry. The 3D modeling files can be found in Supplementary Material S1. Following initial modeling, the designs were optimized and repaired with Materialise Magics 24.0 (Materialise N.V., Belgium) to ensure suitability for three-dimensional (3D) printing. The raw materials utilized included highly spherical metal powders with particle sizes between 15 and 53 μm, specifically radio frequency plasma-spheroidized tantalum powder and plasma rotating electrode-atomized Ti6Al4V powder. The particle size distribution was assessed using a laser diffraction particle size analyzer. The scaffolds were fabricated by Ningxia Orient Additive Manufacturing Technology Co., Ltd., utilizing an FS271M laser powder bed fusion system (Farsoon Technologies Co., Ltd., China). To mitigate oxidation, all fabrication processes were conducted in an argon atmosphere, with the oxygen concentrations maintained below 100 ppm. A 67° layer rotation scanning strategy was implemented during printing to reduce residual stress accumulation between adjacent layers.

Optimized processing parameters were employed to produce high-density porous scaffolds. For tantalum scaffolds, the parameters included a laser power of 340 ± 5 W, a scanning speed of 530 ± 5 mm/s, a hatch spacing of 100 μm, and a layer thickness of 30 μm. For titanium alloy (Ti6Al4V) scaffolds, the parameters included a laser power of 280 ± 5 W, a scanning speed of 650 mm/s, a hatch spacing of 90 μm, and a layer thickness of 40 μm. Upon completion of fabrication, the scaffolds were detached from the build platform using wire electrical discharge machining. Residual and partially sintered powders were removed via sandblasting, followed by ultrasonic cleaning in ethanol. Finally, post-fabrication annealing was conducted to alleviate residual thermal stresses induced during the laser powder bed fusion process. The tantulum scaffolds were vacuum-annealed at 1200°C for 2 h, while

the Ti6Al4V scaffolds underwent annealing at 800°C for the same duration under identical atmospheric conditions.

Cylindrical scaffolds measured 7 mm in both diameter and height, while disc-shaped scaffolds measured 15 mm in diameter and 1 mm in height. Surface morphology and microstructure were examined using scanning electron microscopy (SEM), and energy-dispersive spectroscopy was used to qualitatively analyze surface elemental composition.

### 2.2. Static mechanical testing

To assess the mechanical properties of the scaffolds both before and after implantation, as well as to monitor their temporal changes, uniaxial compression tests were performed using a universal testing machine (CMT4000, MTS SYSTEMS Co., Ltd., China). These tests were conducted on scaffold samples prior to implantation and again after a two-month *in vivo* period. Load–displacement data were recorded and subsequently converted into stress–strain curves, from which the elastic modulus and yield strength were derived. Three samples from each group were tested.

### 2.3. *In vitro* evaluation of bone marrow-derived mesenchymal stem cell–scaffold interactions

Disc-shaped samples (φ15 mm × 1 mm) were used for *in vitro* co-culture experiments. Rabbit BMSCs ($2 \times 10^4$ cells per well) were seeded onto the surfaces of both scaffolds in 12-well plates. Cell proliferation was assessed on days 1, 3, and 5 using the Cell Counting Kit-8 (CCK-8; Biyuntian, China). Scaffold cytotoxicity was evaluated on day 1 using a live/dead cell staining kit (C2015S, Biyuntian, China). Cell adhesion to the scaffold surfaces was examined using SEM, as well as phalloidin and 4',6-diamidino-2-phenylindole (DAPI) fluorescence staining (Biyuntian, China). These analyses were performed to comprehensively assess the biocompatibility of the two scaffold types.

### 2.4. Alkaline phosphatase activity and mineralized nodule staining

A total of $1 \times 10^5$ BMSCs were seeded onto the surfaces of both scaffolds in six-well plates. After 24 h of culture, the medium was replaced with osteogenic induction medium (OriCell, China), which was refreshed every three days. Alkaline phosphatase (ALP) activity was measured on days 3, 5, and 7 using an ALP assay kit (C3206, Biyuntian, China). On days 14 and 21, osteogenic mineralization was evaluated using alizarin Red S staining (ARS; OriCell, China) to assess the osteogenic differentiation capacity of BMSCs on the scaffolds.

### 2.5. Real-time quantitative polymerase chain reaction

To evaluate the expression of osteogenic-related genes in co-cultured cells, $1 \times 10^5$ BMSCs were seeded onto the surfaces of both scaffolds in 12-well plates. Total RNA was extracted at days 3, 7, and 14 of induction using the FreeZol reagent kit ( R711-01/02, Vazyme, China). Complementary DNA (cDNA) was synthesized using a reverse transcription kit (R233-01, Vazyme, China). Quantitative real-time polymerase chain reaction (qRT-PCR) was conducted using a real-time PCR system under the following cycling conditions: 95°C for 30 s, followed by 45 cycles of 95°C for 5 s and 60°C for 34 s. Relative messenger RNA (mRNA) expression levels of osteogenic genes—*Bmp2*, *Col1a1*, *Runx2*, *Ocn*, and *Ogn*—were calculated using the $2^{-\Delta\Delta Ct}$ method. All primers were synthesized by Wuhan JinKaiRui Bioengineering Co., Ltd. (China), and their sequences are listed in Table 1.

### 2.6. Western blot

To evaluate the expression of proteins related to the bone morphogenetic protein 2 (BMP2)–Smad signaling pathway, BMSCs were co-cultured with PTi and PTa scaffolds for seven days. Total protein was extracted using a protein extraction kit and quantified using a bicinchoninic acid (BCA) assay (both from keyGEN BioTECH, China). Equal amounts of protein were separated via 10% sodium dodecyl sulfate (SDS)-polyacrylamide gel electrophoresis (Epizyme, China) and transferred onto methanol-activated polyvinylidene fluoride membranes. Membranes were blocked with 5% skim milk for 2 h at room temperature, followed by overnight incubation at 4°C with primary antibodies against BMP-2, SMAD1, phosphorylated (p)-

**Table 1. Primers used for quantitative real-time polymerase chain reaction analysis**

| Gene | Forward primer sequence (5'–3') | Reverse primer sequence (5'–3') |
|---|---|---|
| *Gapdh* | TGAAGGTCGGAGTGAACGGAT | CGTTCTCAGCCTTGACCGTG |
| *Runx2* | TCGCCTCACAAACAACCACAG | CTGGTAGTGACCTGCGGAGATT |
| *Bmp2* | GGTGGAACGACTGGATTGTG | CGGAATCTTAGAGTTCACGGAGT |
| *Ocn* | CTCACTCTTGTCGCCCTGCT | CTCTTGGACACGAAGGCTGAG |
| *Ogn* | GCAGATCATTTGGAAGAAGCCA | CACATAGCAAGCAAGTGGGC |
| *Col1a1* | CAAGAACGGAGATGACGGAGAA | CATCCAAACCACTGAAACCTCTGT |

SMAD1/5/9, Runt-related transcription factor 2 (RUNX2), and glyceraldehyde 3-phosphate dehydrogenase (GAPDH; Abcam, United States of America). After three 10-minute washes with Tris-buffered saline with Tween-20, membranes were incubated with horseradish peroxidase-conjugated secondary antibodies (1:5000; Affinity, China) for 2 h at room temperature. Protein bands were visualized using an automated fluorescence detection system.

### 2.7. Rabbit femoral defect model and scaffold implantation

All animal experiments complied with the relevant laws and regulations governing animal research in China and were approved by the Ethics Committee of Ningxia Medical University (approval number IACUC-NYLAC-2024-049). A total of 54 male New Zealand White rabbits (6–8 weeks old, 3.1 ± 0.5 kg) were randomly assigned to four groups: blank (periosteum exposed without treatment), defect (bone defect created without scaffold implantation), PTi scaffold, and PTa scaffold groups.

Following anesthesia, a 2.5 cm longitudinal incision was made along the axis of the distal femur (Animal modeling hollow drills can be found in Supplementary Material S2). A cylindrical bone defect (8 mm in diameter) was created using an orthopedic hollow drill, and sterilized PTi or PTa scaffolds were implanted accordingly. After implantation, the site was rinsed with hydrogen peroxide and saline, disinfected with iodine tincture, and closed in layers with sutures. A pressure dressing with sterile gauze was applied. All procedures were conducted in a standardized surgical environment at the Animal Center of Ningxia Medical University. X-ray imaging was performed at four and eight weeks post-implantation to evaluate implant stability.

### 2.8. Histological staining: hematoxylin and eosin, Masson's trichrome, and toluidine blue

At four and eight weeks post-implantation, rabbits in each group were euthanized, and the scaffolds, along with surrounding tissues, were harvested. The specimens were fixed in 4% paraformaldehyde, followed by dehydration through a graded ethanol series. After paraffin embedding, hard tissue sections were prepared. These sections were subsequently stained with hematoxylin and eosin (H&E), Masson's trichrome, and toluidine blue, then examined under a light microscope.

### 2.9. Transcriptomic analysis

At four weeks post-implantation, the experimental rabbits were euthanized, and bone tissue surrounding the implanted scaffolds was harvested and immediately flash-frozen in liquid nitrogen. The samples were ground into a fine powder, and total RNA was extracted using an RNA purification kit (TaKaRa Biomedicals, Japan). RNA purity and integrity were assessed using a NanoDrop 2000 spectrophotometer (Thermo Fisher Scientific, United States of America) and an Agilent 2100 Bioanalyzer (United States of America) or LabChip GX system (PerkinElmer, United States of America). Following quality assessment, cDNA libraries were constructed and evaluated using a Qsep400 high-throughput analyzer (Bioptic, China). Libraries that passed quality control were subjected to paired-end 150 base pair (PE150) sequencing on a high-throughput sequencing platform.[11,12]

### 2.10. Proteomic analysis

The method for bone tissue sample collection was consistent with that used in the transcriptomic analysis. Tissues were lysed in buffer containing 1% SDS and 1% protease inhibitor, followed by ultrasonic disruption. Protein concentrations were measured using a BCA protein assay kit. Equal amounts of protein from each group were enzymatically digested with trypsin using the filter-aided sample preparation method.

The resulting peptides were dissolved in mobile phase A (0.1% formic acid and 2% acetonitrile in water) and separated using a NanoElute ultra-high-performance liquid chromatography system (Bruker Daltonics, Germany). Peptides were subsequently ionized via a CaptiveSpray ion source and analyzed using a timsTOF Pro mass spectrometer (Bruker Daltonics, Germany). Data were acquired in data-independent acquisition mode using parallel accumulation–serial fragmentation.[13,14]

### 2.11. Bioinformatics analysis

We performed bioinformatics analyses on both RNA-sequencing and proteomics datasets. Differential expression analysis of the transcriptomic data was conducted using the DESeq R package (version 1.10.1) to identify differentially expressed genes (DEGs), while proteomic data were analyzed to identify differentially expressed proteins (DEPs). The screening criteria for DEGs were a false discovery rate <0.05 and fold change (FC) ≥1.5. For DEPs, the criteria were $p < 0.05$ and FC ≥ 1.2. Principal component analysis (PCA) was used to assess sample clustering within each group. Venn diagrams and volcano plots were employed to visualize upregulated and downregulated DEGs and DEPs. Gene Ontology (GO) and Kyoto Encyclopedia of Genes and Genomes (KEGG) enrichment analyses of DEGs were performed using the ClusterProfiler package (v3.8.1).[15] Finally, osteogenesis-related DEGs and DEPs were screened, and the top 50 candidates were subjected to protein–protein interaction (PPI) network analysis.

### 2.12. Statistical analysis

All data are expressed as mean ± standard deviation. Statistical analyses were performed using GraphPad Prism 8.0 (GraphPad Software, United States of America). For comparisons between two groups, unpaired two-tailed Student's *t*-tests were conducted. For comparisons among multiple groups, one-way analysis of variance followed by Tukey's post hoc test was used. A *p*-value <0.05 was considered statistically significant.

## 3. Results

### 3.1. Comprehensive characterization of porous tantalum and porous titanium alloy scaffolds

A comprehensive characterization of the fabricated PTi6Al4V (PTi) and PTa scaffolds—including their design architecture, microstructural morphology, elemental composition, and mechanical properties—is presented in Figure 1.

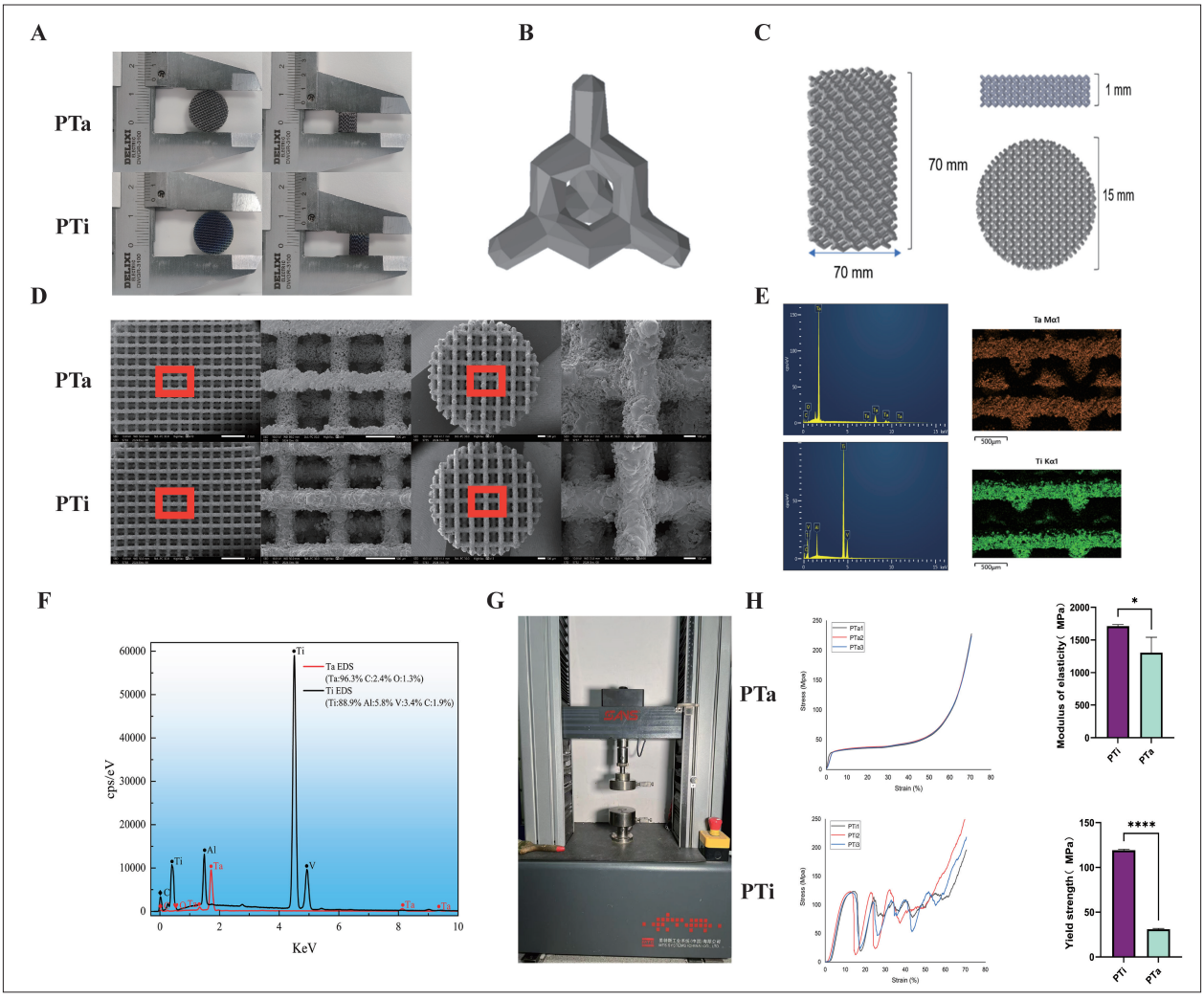


**Figure 1.** Design and characterization of PTa and porous titanium alloy (PTi6Al4V) scaffolds. (A) Photographs of the fabricated PTa and PTi scaffolds. (B) Illustration of the diamond lattice unit cell structure employed in the scaffold design. (C) Schematic showing the design parameters of cylindrical and disc-shaped scaffolds. (D) Scanning electron microscopy images showing the surface morphology and microstructural features of both scaffold types, with PTa exhibiting a rougher surface topology than PTi. Magnifications = 10×, 50×; scale bars: 2 μm, 500 μm. (E and F) EDS results showing the surface elemental composition: PTa scaffolds were primarily composed of tantalum (Ta; 96.3%), whereas PTi scaffolds contained titanium (Ti; 88.9%), aluminum (Al; 5.8%), and vanadium (V; 3.4%). Magnification = 50×; scale bar: 500 μm. (G and H) Stress–strain curves obtained from compression testing of both scaffold types, with the calculated elastic modulus and yield strength indicating that PTa has a lower modulus (1.3 ± 0.2 GPa) and significantly lower yield strength (30 ± 0.8 MPa) compared to PTi (1.7 ± 0.04 GPa and 119 ± 1 MPa, respectively), though more closely matching that of human cancellous bone. Abbreviations: C, carbon; O, oxygen; PTa, porous tantalum; EDS, energy-dispersive spectroscopy.

Photographs of the PTi and PTa scaffolds are shown in Figure 1A, and the diamond lattice unit cell structure employed for both scaffold types is illustrated in Figure 1B. The geometric dimensions of the cylindrical and disc-shaped scaffolds are detailed in Figure 1C.

SEM images (Figure 1D) revealed that both PTi and PTa scaffolds possessed a consistent 3D porous structure. At higher magnification, the surface of the PTa scaffold appeared notably rougher than that of PTi, which may facilitate enhanced cell adhesion. Energy-dispersive spectroscopy analysis (Figure 1E and 1F) confirmed that PTa scaffolds were primarily composed of tantalum, whereas PTi scaffolds contained titanium (88.9%), aluminum (5.8%), and vanadium (3.4%).

Stress–strain curves for both scaffold types are depicted in Figure 1G–1H. The elastic modulus of the PTa scaffold was slightly lower (1.3 ± 0.2 GPa) than that of the PTi scaffold (1.7 ± 0.04 GPa). Force-displacement curves for both types of brackets can be found in Supplementary Material S3. Notably, although the PTa scaffold exhibited a significantly lower yield strength (30 ± 0.8 MPa) compared to the PTi scaffold (119 ± 1 MPa), its mechanical strength is closer to that of human cancellous bone, potentially offering improved biomechanical compatibility in bone tissue regeneration applications.

### 3.2. *In vitro* evaluation of rabbit bone marrow-derived mesenchymal stem cell co-cultured with porous tantalum and porous titanium alloy scaffolds

To comprehensively evaluate the *in vitro* biocompatibility and osteogenic potential of PTa and PTi scaffolds, a series of experiments was conducted to assess BMSC viability, proliferation, adhesion, and osteogenic differentiation (Figure 2).

Live/dead staining was used to assess the viability of BMSCs co-cultured with PTa and PTi scaffolds. Fluorescence microscopy revealed a predominance of green fluorescence in the control, PTi, and PTa groups, indicating high cell viability across all groups. Only minimal red fluorescence was observed, suggesting that both scaffold types exhibited negligible cytotoxicity (Figure 2A). Cell proliferation was evaluated using the CCK-8 assay. Compared to the control group, BMSCs cultured on the PTa scaffold showed significantly increased proliferation at days 1 and 3 relative to those on the PTi scaffold. By day 5, no significant difference in proliferation was observed between the PTa and PTi groups, indicating a similar long-term proliferative capacity (Figure 2B).

SEM imaging on day 1 revealed the morphology and adhesion of BMSCs on the surfaces of both scaffolds. Cells exhibited good spreading and attachment on both materials (Figure 2C). Furthermore, confocal microscopy following phalloidin (for F-actin) and DAPI (for nuclei) staining demonstrated a higher density of adherent cells on the PTa scaffold compared to the PTi scaffold, suggesting superior initial cell attachment on PTa (Figure 2D).

### 3.3. Evaluation of osteogenic differentiation potential

Rabbit BMSCs were co-cultured with PTi and PTa scaffolds and subjected to osteogenic induction for three, five, and seven days. ALP staining and corresponding quantitative analysis were performed at each time point (Figure 2E). The results demonstrated that ALP activity in the PTa group was consistently higher than that in the PTi group across all time points, indicating that PTa scaffolds promoted enhanced early osteogenic differentiation. To determine late-stage osteogenesis, ARS staining was conducted on days 14 and 21 to evaluate mineralized nodule formation (Figure 2F). The PTa group exhibited a significantly greater number of mineralized nodules than the PTi group at both time points, suggesting a superior osteogenic mineralization capacity of the PTa scaffolds.

### 3.4. Expression of osteogenesis-related genes

The relative mRNA expression levels of osteogenic markers—*Bmp2*, *Col1a1*, *Runx2*, *Ocn*, and *Ogn*—were evaluated on days 3, 7, and 14 of BMSC co-culture with PTa and PTi scaffolds. GAPDH served as the internal control, and expression levels in the control group were normalized to 1.00. The $2^{-\Delta\Delta Ct}$ method was used to calculate the relative expression of target genes in the PTi and PTa groups. On day 3, *Bmp2*, *Col1a1*, and *Runx2* expression levels were significantly upregulated in the PTa group compared to the PTi group, while OCN and OGN showed no significant differences. On day 7, the PTa group exhibited significantly higher expression of all five osteogenic genes. By day 14, the expression levels of all genes showed no significant differences between the two groups (Figure 2G). These findings suggest that the PTa scaffold may promote the early expression of osteogenesis-related genes, potentially contributing to its enhanced osteoinductive capacity during the initial stages of bone regeneration.

### 3.5. Evaluation of BMP-2/SMAD1/RUNX2 signaling pathway activation

After 7 days of co-culture of BMSCs with PTa and PTi scaffolds, the expression levels of BMP-2, SMAD1, p-SMAD1/5/9, and RUNX2 proteins were evaluated using Western blotting. Band intensities were quantified with ImageJ software (National Institutes of Health, United States of America), and the p-SMAD1/5/9 to SMAD1 ratio was calculated for each group. All experiments were performed in triplicate, and the resulting data were statistically analyzed. The results demonstrated that the

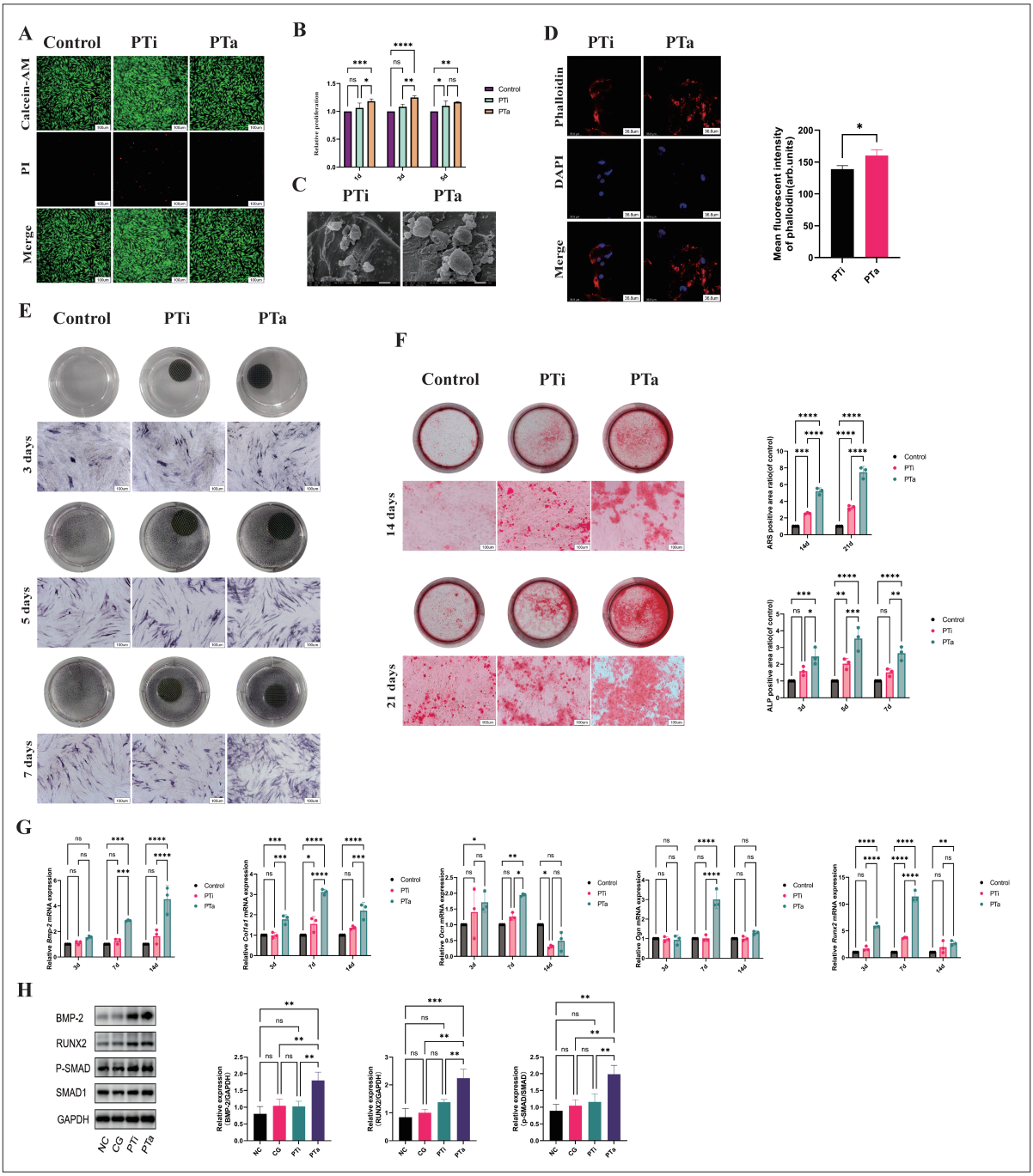


**Figure 2.** *In vitro* cellular responses of rabbit BMSCs co-cultured with porous tantalum (PTa) and porous titanium alloy (Pti) scaffolds. (A) Live/dead staining of BMSCs after 1 day of co-culture with PTa and PTi scaffolds, indicating high cell viability. (B) Cell Counting Kit-8 assay showing the relative proliferation of BMSCs on days 1, 3, and 5. (C) Scanning electron microscopy images showing BMSC adhesion and morphology on the scaffold surfaces after one day. Magnification = 8000×; scale bar: 2 μm. (D) Confocal microscopy images showing F-actin (phalloidin; red) and nuclei (DAPI; blue) staining to evaluate cytoskeletal organization and cell attachment. Magnification = 600×; scale bar: 36.8 μm. (E) ALP staining and semi-quantitative analysis on days 3, 5, and 7 post-osteogenic induction to assess early osteogenic differentiation. Magnification = 10×; scale bar: 100 μm. (F) ARS staining and quantification of mineralized matrix formation on days 14 and 21. Magnification = 10×; scale bar: 100 μm. (G) mRNA expression levels of osteogenic genes (*Bmp2*, *Col1a1*, *Runx2*, *Ocn*, and *Ogn*) on days 3, 7, and 14, normalized to *Gapdh*. (H) Western blot analysis of BMP-2, SMAD1, phosphorylated SMAD1/5/9 (p-SMAD1/5/9), and RUNX2 proteins at day 7, indicating activation of the BMP-2/SMAD1/RUNX2 signaling pathway. Abbreviations: AM, acetoxymethyl; arb., arbitrary; CG, defect control group; d, days; GAPDH, glyceraldehyde 3-phosphate dehydrogenase; NC, normal control group; ns, not significant; PI, propidium iodide; BMSCs, bone marrow-derived mesenchymal stem cells; DAPI, 4',6-diamidino-2-phenylindole; ALP, alkaline phosphatase; ARS, Alizarin red S; mRNA, relative messenger RNA; BMP-2, bone morphogenetic protein 2; RUNX2, runt-related transcription factor.

expression levels of BMP-2, SMAD1, p-SMAD1/5/9, and RUNX2 were significantly upregulated in the PTa group compared to the PTi group (Figure 2H), indicating that PTa scaffolds more effectively activate the BMP-2/SMAD1/RUNX2 signaling pathway. This enhanced signaling activity may underlie the superior osteoinductive potential observed in the PTa group.

### 3.6. Postoperative recovery and histological evaluation of bone regeneration

A thorough assessment of *in vivo* bone regeneration, including postoperative recovery, implant fixation, and histological analysis, was performed to evaluate the osteogenic efficacy of PTa and PTi scaffolds (Figure 3).

All rabbits regained consciousness within 2 h following surgery. The local incisions healed well, without signs of inflammation, infection, or wound dehiscence. X-ray imaging at four and eight weeks postoperatively confirmed that the implants remained properly fixed at the defect sites (Figure 3A).

To assess bone regeneration at the microscopic level, histological staining was performed at four and eight weeks after implantation. H&E, Masson's trichrome, and toluidine blue staining revealed substantial new bone formation within the defect regions in both PTa and PTi scaffold groups (Figure 3B–3G). Notably, the PTa group demonstrated more pronounced new bone tissue formation and superior bone ingrowth compared to the PTi group, indicating a stronger osteogenic capacity associated with the PTa scaffolds.

### 3.7. Comparative transcriptomic analysis of porous tantalum and porous titanium alloy scaffold-induced bone regeneration

Comprehensive lists of all identified proteins and genes from the proteomic and RNA-seq analyses are available in Supplementary File 2. To further elucidate the osteogenic mechanisms associated with PTa and PTi scaffolds, RNA sequencing was conducted on bone tissue samples collected one month after implantation(Figure 4). The

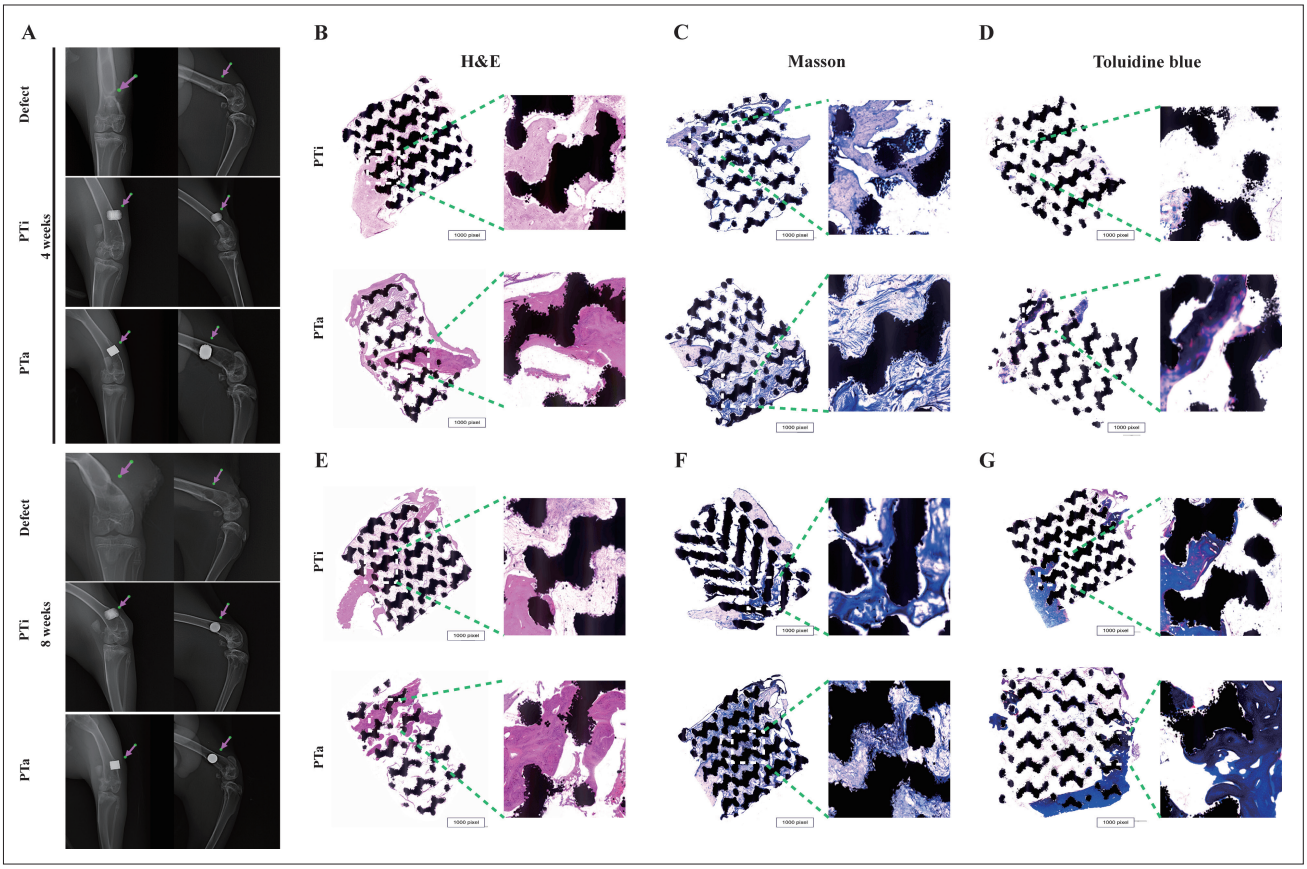


**Figure 3.** *In vivo* histological evaluation of bone regeneration induced by porous tantalum (PTa) and porous titanium alloy (PTi) scaffolds. (A) Representative X-ray images at four and eight weeks post-implantation in the rabbit femoral defect model, showing stable scaffold fixation. Histological staining at four weeks, including (B) hematoxylin and eosin (H&E), (C) Masson's trichrome, and (D) toluidine blue, reveals new bone formation in both groups. Histological staining at eight weeks using (E) H&E, (F) Masson's trichrome, and (G) toluidine blue demonstrates more extensive bone ingrowth into the PTa scaffold compared to the PTi scaffold.

study encompassed four groups: a normal control group (NC, representing healthy bone), a defect group (CG, comprising newly regenerated bone at the defect site), and two scaffold groups (PTa and PTi, representing new bone formation surrounding each respective scaffold). Each group consisted of six biological replicates.

Principal component analysis (Figure 4A) demonstrated a distinct separation among the groups, signifying unique transcriptomic profiles. The Venn diagram (Figure 4B) depicts both the overlap and distinctiveness of DEGs across the comparisons. Pearson correlation analysis (Figure 4C) corroborated strong intra-group consistency and pronounced inter-group differences. Volcano plots and hierarchical clustering heatmaps (Figure 4D and 4E) further underscored significant variations in gene expression patterns. A total of 2459 DEGs were identified between the PTa and PTi groups, with an FC of ≥ 1.5 and a false discovery rate of < 0.05. These DEGs underwent GO and KEGG enrichment analyses (Figure 4F–4I). GO analysis revealed enrichment in processes such as integrin-mediated signaling, glycolysis, and phagocytosis. Notably, genes upregulated in the PTi group were linked to neutrophil chemotaxis, innate immunity, and adaptive immune responses. KEGG analysis indicated significant enrichment in the mitogen-activated protein kinase signaling pathway, osteoclast differentiation, and chemokine signaling pathways.

To elucidate the principal regulators implicated in PTa-mediated osteogenesis, a PPI network analysis was subsequently performed on both transcriptome-derived DEGs and proteome-identified DEPs associated with osteogenesis (Figure 6). This analysis identified several hub genes, including *Col1a1*, *Spp1*, *Col3a1*, *Mmp9*, and *Acan*, which are intricately linked to collagen synthesis, osteoblast adhesion and mineralization, bone remodeling, and angiogenesis (Figure 6E and 6G). These results imply that PTa may facilitate bone regeneration through the coordinated regulation of extracellular matrix production, cellular adhesion, and remodeling pathways.

To enhance the validation and complementarity of the transcriptomic findings at the protein level, a proteomic analysis was subsequently performed to investigate differential protein expression patterns and the associated biological processes between the PTa and PTi scaffolds.

### 3.8. Comparative proteomic analysis of porous tantalum and porous titanium alloy scaffold-induced bone regeneration

Proteomic analysis was conducted utilizing the same sample cohorts as employed in the RNA-sequencing investigation. PCA (Figure 5A) demonstrated distinct clustering among the four groups, indicative of divergent proteomic profiles. Pearson correlation analysis (Figure 5B) confirmed strong intra-group consistency. A bar chart (Figure 5C) illustrates the number of DEPs identified between the groups. Heatmaps and volcano plots (Figure 5D and 5E) further revealed distinct protein expression patterns across the groups. Subsequent GO and KEGG enrichment analyses were performed on the DEPs (Figure 5F–5I). GO analysis indicated that the DEPs between the PTa and PTi groups were predominantly associated with biological regulation, primary metabolic processes, anatomical structure development, and signal transduction. KEGG pathway analysis demonstrated significant enrichment of these DEPs in pathways related to phagosomes, lysosomes, nuclear factor kappa-light-chain-enhancer of activated B cell signaling, nucleotide oligomerization domain-like receptor signaling, and the catabolism of branched-chain amino acids (valine, leucine, and isoleucine).

In the PTi group, upregulated proteins were significantly enriched in pathways related to immune responses and cell proliferation, including the erythroblastic oncogene B signaling pathway, B cell receptor signaling pathway, and phosphoinositide 3-kinase–protein kinase B signaling pathway. A PPI network analysis of osteogenesis-associated DEPs (Figure 6A and 6C) identified several key regulators potentially involved in PTa-induced bone regeneration, such as Ras-related C3 botulinum toxin substrate 2 (RAC2), caveolin-1 (CAV1), annexin A1 (ANXA1), Ras homolog gene family, member B (RHOB), and integrin subunit alpha 1 (ITGA1). These findings suggest that the superior osteogenic potential of PTa scaffolds may be attributed to enhanced cell adhesion, signal transduction, chromatin remodeling, and cytoskeletal reorganization.

## 4. Discussion

This study elucidates, through comprehensive *in vitro* and *in vivo* experiments, that PTa scaffolds facilitate bone regeneration by providing mechanical support and modulating various biological processes. By employing integrated transcriptomic and proteomic analyses of peri-implant bone tissue within a rabbit model, we gained new insights into the molecular mechanisms underpinning PTa-induced osseointegration. While prior studies have investigated the biological performance of PTa scaffolds, most have focused on individual pathways or cellular behaviors.[16–18] Few studies have applied integrated multi-omics approaches. Our findings suggest that PTa scaffolds promote bone regeneration through advantageous physical properties combined with the activation of specific molecular pathways, which may act synergistically to enhance osseointegration and new bone formation.

To our knowledge, this study represents the first systematic investigation of the *in vivo* osteogenic

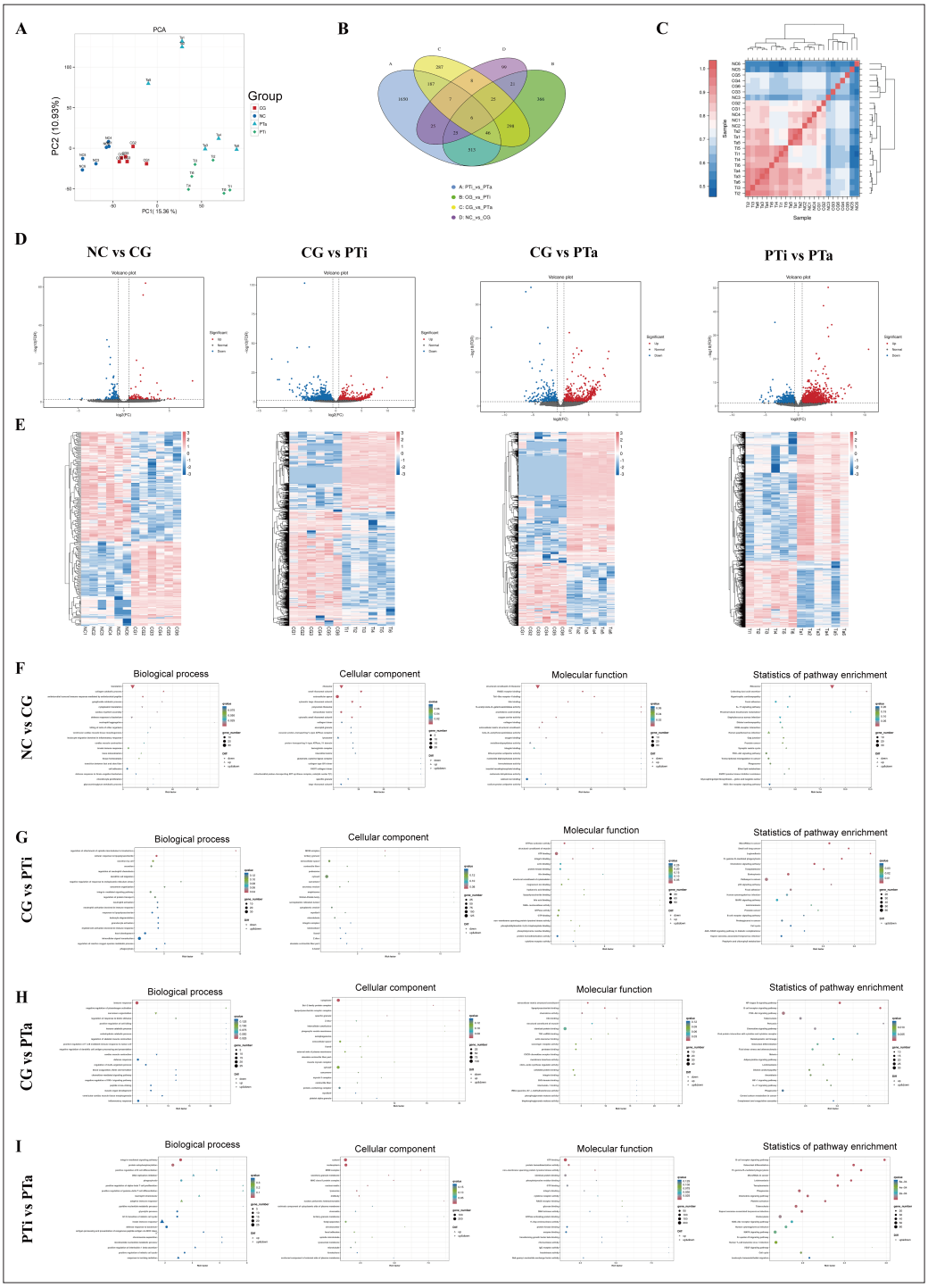


**Figure 4.** Transcriptomic profiling and comparative analysis of bone tissue surrounding porous tantalum (PTa) and porous titanium alloy (PTi) scaffolds. (A) Principal component analysis (PCA) reveals distinct clustering of samples from the normal control (NC), defect control (CG), PTi, and PTa groups, indicating divergent transcriptomic signatures. (B) Venn diagram illustrating the overlap and uniqueness of differentially expressed genes (DEGs) among the groups. (C) Pearson correlation heatmap showing strong intra-group consistency and clear inter-group distinctions. (D) Volcano plot and (E) hierarchical clustering heatmap highlighting DEGs between the PTa and PTi groups. (F) Gene Ontology (GO) and Kyoto Encyclopedia of Genes and Genomes (KEGG) enrichment analyses of DEGs between the NC and CG groups, identifying biological processes associated with bone defect response. (G) GO and KEGG enrichment analyses comparing the CG and PTi groups, revealing enrichment of immune and inflammatory pathways in PTi. (H) GO and KEGG enrichment analyses comparing the CG and PTa groups, indicating enhanced osteogenic and metabolic pathways in PTa. (I) GO and KEGG enrichment of DEGs between the PTi and PTa groups, showing key differences in osteogenesis, immune modulation, and cell signaling processes.

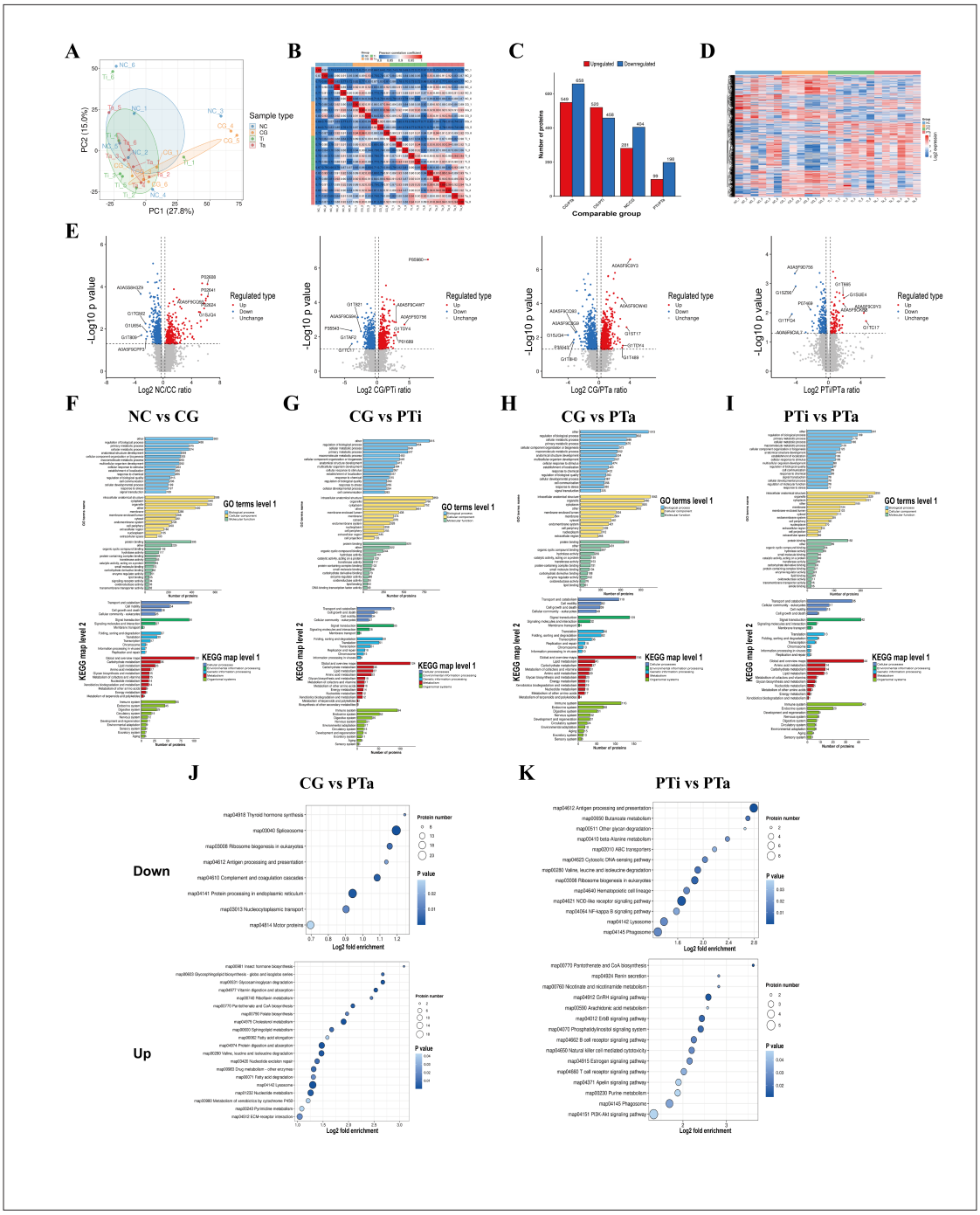


**Figure 5.** Proteomic profiling and comparative analysis of peri-implant bone tissues in different scaffold groups. (A) Principal component analysis (PCA) revealed distinct clustering among normal control (NC), defect control (CG), porous titanium alloy (PTi), and porous tantalum (PTa) groups, indicating divergent proteomic profiles. Pearson correlation coefficient (B) heatmaps and (C) bar chart confirm high intra-group consistency and distinct inter-group variation. (D) Hierarchical clustering heatmap of differentially expressed proteins (DEPs) across all groups. (E) Volcano plots highlighting significantly upregulated and downregulated proteins between groups. (F) Gene Ontology (GO) and Kyoto Encyclopedia of Genes and Genomes (KEGG) enrichment analyses of DEPs between NC and CG groups revealed biological processes related to bone defect responses. (G) GO and KEGG analyses comparing the CG and PTi groups demonstrate enrichment in immune-related pathways. (H) GO and KEGG analyses of CG vs. PTa groups indicate activation of osteogenic, metabolic, and angiogenic pathways. (I) Comparative GO and KEGG analysis between PTi and PTa groups reveals distinct molecular mechanisms underlying bone regeneration. (J) Bubble plots of the top 20 upregulated and downregulated KEGG pathways in PTa vs. CG, showing osteogenesis- and repair-associated signaling activation. (K) Bubble plots of the top 20 upregulated and downregulated KEGG pathways in PTa vs. PTi, emphasizing enhanced bone formation and immune modulation in PTa.

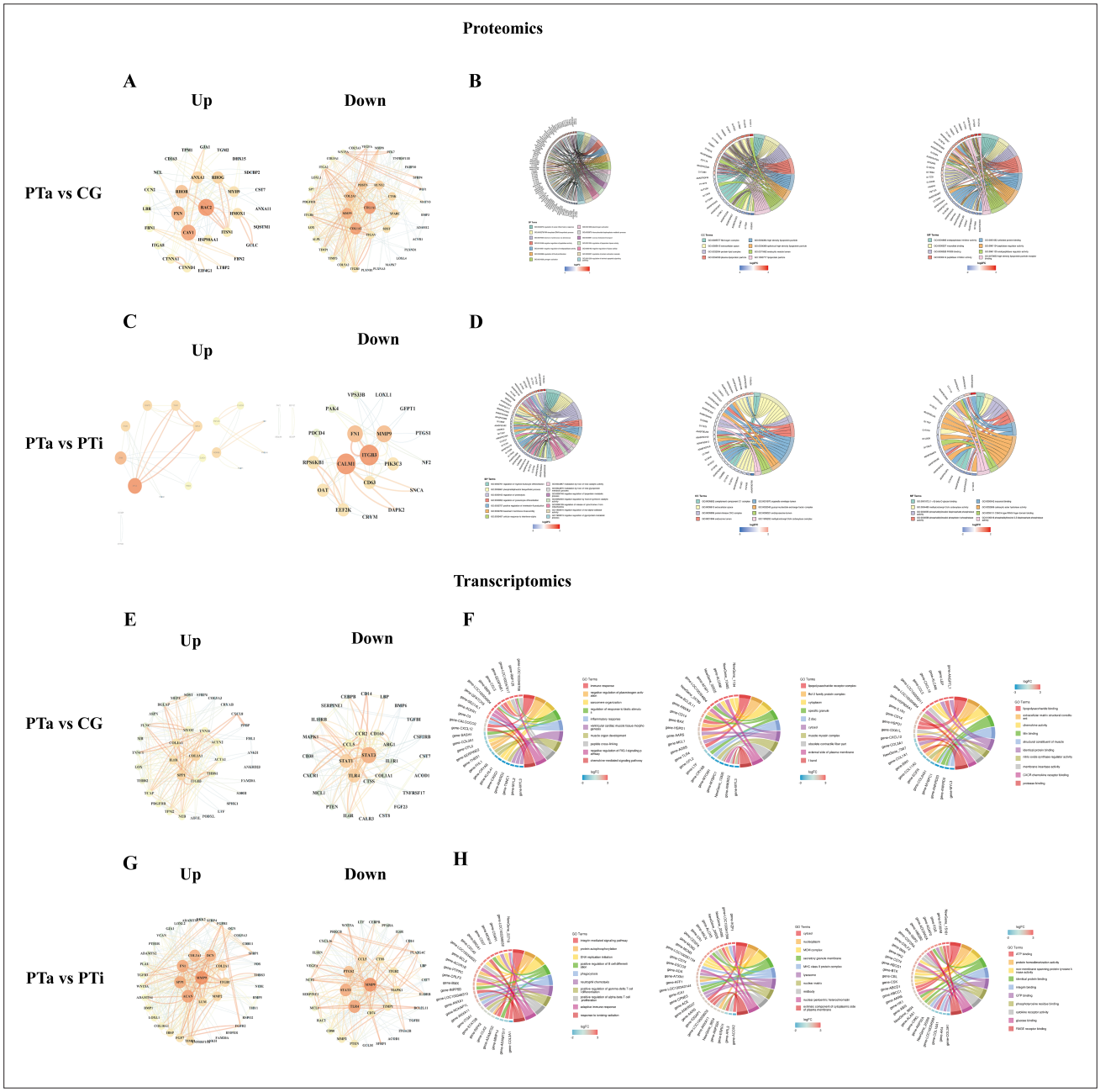


**Figure 6.** Protein–protein interaction (PPI) networks and Gene Ontology (GO) enrichment chord plots of differentially expressed proteins (DEPs) and genes (DEGs). (A) PPI network of the top 50 upregulated and downregulated osteogenesis-related DEPs between the porous tantalum (PTa) and defect control (CG) groups. (B) GO enrichment chord diagram displaying biological processes associated with DEPs between the PTa and CG groups. (C) PPI network of the top 50 upregulated and downregulated osteogenesis-related DEPs between PTa and porous titanium alloy (PTi) groups. (D) GO enrichment chord diagram illustrating the relationship between DEPs and enriched biological functions in the PTa vs. PTi comparison. (E) PPI network of the top 50 upregulated and downregulated osteogenesis-related DEGs between the PTa and CG groups. (F) GO enrichment chord diagram showing biological processes linked to DEGs in the PTa vs. CG comparison. (G) PPI network of the top 50 upregulated and downregulated osteogenesis-related DEGs between the PTa and PTi groups. (H) GO enrichment chord diagram visualizing functional associations of DEGs between PTa and PTi groups.

mechanisms of PTa and PTi scaffolds utilizing integrated transcriptomic and proteomic analyses. We also performed a direct comparison of the biological responses elicited by these two materials. Given the complexity of the physiological environment and the multifactorial nature of bone regeneration, the clinical translation of PTa scaffolds remains a long-term objective.[19] Nevertheless, our findings provide significant evidence supporting the potential application of PTa in bone tissue engineering.

Extensive and complex bone defects remain a major challenge in orthopedic treatment.[20] Although autologous bone grafting is regarded as the gold standard, its application is limited by the scarcity of donor tissue and complications associated with graft harvesting.[21] Metal-based implants have emerged as promising alternatives for the reconstruction of large bone defects. Materials such as stainless steel and titanium alloys are widely used in clinical settings due to their favorable mechanical properties.[22,23] However, their relatively high elastic modulus may lead to stress shielding, which can result in bone resorption and impaired osseointegration over time.[24]

The introduction of PTa represents a significant advancement in the development of metallic biomaterials. Compared with traditional metallic implants, such as titanium alloys, PTa demonstrates enhanced corrosion resistance, higher friction coefficients, and superior wear resistance.[25] Moreover, the elastic modulus and mechanical strength of PTa are closely aligned with those of cancellous bone, which helps reduce stress shielding while offering sufficient biomechanical support.[26] Nevertheless, the high melting point and density of tantalum have historically presented substantial challenges in its processing and clinical application. The rapid progress in additive manufacturing has facilitated the emergence of 3D-printed PTa as a next-generation implant material. This technology allows for precise and customizable fabrication of intricate implant geometries with high resolution and integration. When combined with computed tomography (CT)-based 3D modeling, 3D-printed PTa holds significant promise for applications in the treatment of complex bone defects.[27]

In addition, to address the mechanical and functional requirements of bone repair, various strategies have been developed for modifying the surface properties of metallic alloys. A prevalent method involves applying tantalum coatings to titanium scaffolds to improve their bioactivity and osseointegration potential.[28] Studies have also shown that incorporating PTa scaffolds with drug delivery systems and targeted therapeutic strategies can mitigate the inherent limitations of the material's mechanical and physicochemical properties, thereby facilitating multifunctional enhancements.[29] Nonetheless, the biological mechanisms through which PTa promotes osteogenesis are not yet fully elucidated and require further investigation.

In this study, PTa and PTi scaffolds with identical specifications were fabricated. Mechanical testing indicated that PTi exhibited a significantly higher elastic modulus and yield strength compared to PTa; however, the elastic modulus of PTa more closely approximated that of human cancellous bone. Moreover, PTa still provided sufficient mechanical strength to support bone tissue. Its highly porous and interconnected architecture facilitates cell adhesion and bone tissue ingrowth, rendering PTa a promising candidate for load-bearing bone integration applications.[27] Subsequent *in vitro* experiments assessed the biocompatibility of PTa by evaluating cytotoxicity, cell adhesion, and proliferation of rabbit BMSCs co-cultured with PTa scaffolds. The results confirmed the excellent biocompatibility of PTa. It is worth noting that, in both the SEM and Phalloidin staining experiments, PTa and PTi scaffolds were used as direct comparators, without including a separate tissue culture plastic control. This design choice was deliberate. The two scaffolds share identical structural parameters but differ in material composition, allowing for a direct evaluation of how the intrinsic physicochemical properties of tantalum versus titanium influence cellular behavior. By contrast, cells grown on smooth tissue culture plastic exhibit fundamentally different adhesion and morphology due to the distinct surface characteristics, which would confound interpretation in the context of scaffold comparison. The osteogenic differentiation potential was further evaluated using ALP activity and ARS, which demonstrated that PTa significantly enhanced the osteogenic differentiation of BMSCs compared to PTi. These findings are consistent with previous reports.[30,31]

Gene expression analysis utilizing RT-qPCR demonstrated that PTa scaffolds significantly upregulated the mRNA expression levels of osteogenic markers, including *Bmp2*, *Col1a1*, *Runx2*, *Ocn*, and *Ogn*, particularly during the initial phases of differentiation. This indicates a superior osteoinductive capacity of PTa compared to PTi. These findings were corroborated by western blot analysis of the BMP-2/SMAD1/RUNX2 signaling pathway, which confirmed enhanced osteogenic signaling in the PTa group. To further validate the *in vivo* efficacy of the scaffolds, PTa and PTi were implanted into rabbit femoral bone defect models. Histological analyses, including H&E, Masson's trichrome, and toluidine blue staining, conducted at four and eight weeks post-implantation, revealed more substantial new bone formation and improved osseointegration in the PTa group relative to the PTi group.

To further elucidate the biological mechanisms underlying PTa-mediated bone regeneration, we conducted integrated transcriptomic (RNA-sequencing) and proteomic (liquid chromatography coupled with tandem mass spectrometry) analyses on peri-implant bone tissues collected one month after surgery. The multi-omics data indicated that PTa promotes bone formation via pathways related to collagen biosynthesis, osteoblast adhesion and mineralization, bone remodeling, angiogenesis, histone acetylation, cytoskeletal dynamics, and cellular metabolism. To pinpoint key molecular regulators involved in PTa-induced osteogenesis, we constructed PPI networks based on both transcriptomic and proteomic osteogenesis-related DEGs and DEPs. Core hub genes (e.g., *Col1a1*, *Spp1*, *Col3a1*, *Mmp9*, Acan) and proteins (e.g., RAC2, CAV1, ANXA1, RHOB, ITGA1) were identified at the transcriptomic and proteomic levels, respectively. These molecules are implicated in essential processes, including extracellular matrix organization, cell adhesion, cytoskeletal remodeling, and intracellular signaling—highlighting their potential roles in mediating the superior osteogenic performance of PTa scaffolds.

While our findings highlight the clinical potential of PTa scaffolds for bone defect repair, additional research is necessary to validate their efficacy in more complex scenarios, such as irregular defect models and patient-specific implants designed using CT-based methodologies. Furthermore, given that PTa is a relatively recent addition to the field of biomaterials, its long-term *in vivo* stability and clinical performance warrant continued investigation.

Overall, this study provides new insights into the osteogenic mechanisms associated with PTa scaffolds. Utilizing integrated multi-omics analysis, we identified specific molecular pathways that contribute to PTa-mediated bone regeneration. These findings not only inform the functional optimization of PTa scaffolds but also lay a scientific foundation for their future clinical translation in addressing complex bone defects.

## 5. Conclusion

This study highlights the promising role of 3D-printed PTa, which demonstrates a remarkable capacity to enhance bone differentiation and ingrowth via multiple biological pathways, rendering it a highly suitable scaffold material for the treatment of complex bone defects.

## Acknowledgments

None.

## Funding

This work was supported by the Key R&D Project of the Ningxia Hui Autonomous Region (Project No. 2021BEG02037), the University-level Fund of Ningxia Medical University (Grant No. XT2024028) and Ningxia Natural Science Foundation (Grant No. 2025 AAC030863).

## Conflict of interest

The authors declare no conflicts of interest.

## Author contributions

*Conceptualization*: Mengxiao Tantai
*Data curation*: Sihao Yu, Zhihai Zhang, and Hui Ma
*Formal analysis*: Chengbin Wang and Tongwei Du
*Funding acquisition*: Zhidong Lu
*Project administration*: Gangning Feng
*Resources*: Junliang Song and Dong Qu
*Visualization*: Yi Zhang
*Writing*: Mengxiao Tantai

## Ethics approval and consent to participate

The animal experiments complied with all relevant laws and regulations governing animal research in China and were approved by the Ethics Committee of Ningxia Medical University (approval number IACUC-NYLAC-2024-049).

## Consent for publication

Not applicable.

## Availability of data

The data generated or analyzed during this study are available from the corresponding author upon reasonable request.

## References

1. Zura R, Xiong Z, Einhorn T, *et al*. Epidemiology of fracture nonunion in 18 human bones. *JAMA Surg*. 2016;151(11):e162775.
doi: 10.1001/jamasurg.2016.2775

2. Miron RJ. Advanced functional materials. *Periodontology 2000*. 2024;94(1):143-160.
doi: 10.1111/prd.12517

3. Zadpoor AA. Current trends in metallic orthopedic biomaterials: from additive manufacturing to bio-functionalization, infection prevention, and beyond. *IJMS*. 2018;19(9):2684.
doi: 10.3390/ijms19092684

4. Arabnejad S, Johnston B, Tanzer M, Pasini D. Fully porous 3D printed titanium femoral stem to reduce stress-

shielding following total hip arthroplasty. *J Orthop Res*. 2017;35(8):1774-1783.
doi: 10.1002/jor.23445

5. Wauthle R, Van Der Stok J, Amin Yavari S, *et al*. Additively manufactured porous tantalum implants. *Acta Biomater*. 2015;14:217-225.
doi: 10.1016/j.actbio.2014.12.003

6. Melancon D, Bagheri ZS, Johnston RB, Liu L, Tanzer M, Pasini D. Mechanical characterization of structurally porous biomaterials built via additive manufacturing: experiments, predictive models, and design maps for load-bearing bone replacement implants. *Acta Biomater*. 2017;63:350-368.
doi: 10.1016/j.actbio.2017.09.013

7. Levine BR, Sporer S, Poggie RA, Della Valle CJ, Jacobs JJ. Experimental and clinical performance of porous tantalum in orthopedic surgery. *Biomaterials*. 2006;27(27):4671-4681.
doi: 10.1016/j.biomaterials.2006.04.041

8. Mao S, Liu Y, Wang F, *et al*. Design and biomechanical analysis of patientspecific porous tantalum prostheses for knee joint revision surgery. *IJB*. 2024;9(4):735.
doi: 10.18063/ijb.735

9. Liu Y, Bao C, Wismeijer D, Wu G. The physicochemical/biological properties of porous tantalum and the potential surface modification techniques to improve its clinical application in dental implantology. *Mater Sci Eng C*. 2015;49:323-329.
doi: 10.1016/j.msec.2015.01.007

10. Sagomonyants KB, Hakim-Zargar M, Jhaveri A, Aronow MS, Gronowicz G. Porous tantalum stimulates the proliferation and osteogenesis of osteoblasts from elderly female patients. *J Orthop Res*. 2011;29(4):609-616.
doi: 10.1002/jor.21251

11. Pertea M, Pertea GM, Antonescu CM, Chang TC, Mendell JT, Salzberg SL. StringTie enables improved reconstruction of a transcriptome from RNA-seq reads. *Nat Biotechnol*. 2015;33(3):290-295.
doi: 10.1038/nbt.3122

12. Love MI, Huber W, Anders S. Moderated estimation of fold change and dispersion for RNA-seq data with DESeq2. *Genome Biol*. 2014;15(12):550.
doi: 10.1186/s13059-014-0550-8

13. Wiśniewski JR, Zougman A, Nagaraj N, Mann M. Universal sample preparation method for proteome analysis. *Nat Methods*. 2009;6(5):359-362.
doi: 10.1038/nmeth.1322

14. Schwanhäusser B, Busse D, Li N, *et al*. Global quantification of mammalian gene expression control. *Nature*. 2011;473(7347):337-342.
doi: 10.1038/nature10098

15. Kanehisa M, Goto S, Sato Y, Furumichi M, Tanabe M. KEGG for integration and interpretation of large-scale molecular data sets. *Nucleic Acids Res*. 2012;40(D1):D109-D114.
doi: 10.1093/nar/gkr988

16. Dou X, Wei X, Liu G, *et al*. Effect of porous tantalum on promoting the osteogenic differentiation of bone marrow mesenchymal stem cells in vitro through the MAPK/ERK signal pathway. *J Orthop Transl*. 2019;19:81-93.
doi: 10.1016/j.jot.2019.03.006

17. Qian H, Lei T, Hua L, *et al*. Fabrication, bacteriostasis and osteointegration properties researches of the additively-manufactured porous tantalum scaffolds loading vancomycin. *Bioact Mater*. 2023;24:450-462.
doi: 10.1016/j.bioactmat.2022.12.013

18. Luo C, Wang C, Wu X, *et al*. Influence of porous tantalum scaffold pore size on osteogenesis and osteointegration: a comprehensive study based on 3D-printing technology. *Mater Sci Eng C*. 2021;129:112382.
doi: 10.1016/j.msec.2021.112382

19. Fan L, Chen S, Yang M, Liu Y, Liu J. Metallic materials for bone repair. *Adv Healthc Mater*. 2024;13(3):2302132.
doi: 10.1002/adhm.202302132

20. Li JJ, Ebied M, Xu J, Zreiqat H. Current approaches to bone tissue engineering: the interface between biology and engineering. *Adv Healthc Mater*. 2018;7(6):1701061.
doi: 10.1002/adhm.201701061

21. Dimitriou R, Jones E, McGonagle D, Giannoudis PV. Bone regeneration: current concepts and future directions. *BMC Med*. 2011;9(1):66.
doi: 10.1186/1741-7015-9-66

22. Bekmurzayeva A, Duncanson WJ, Azevedo HS, Kanayeva D. Surface modification of stainless steel for biomedical applications: revisiting a century-old material. *Mater Sci Eng C*. 2018;93:1073-1089.
doi: 10.1016/j.msec.2018.08.049

23. Kaur M, Singh K. Review on titanium and titanium based alloys as biomaterials for orthopaedic applications. *Mater Sci Eng C*. 2019;102:844-862.
doi: 10.1016/j.msec.2019.04.064

24. Zhang Y, Sun B, Zhao L, Yang G. Design and manufacturing of a novel trabecular tibial implant. *Materials*. 2023;16(13):4720.
doi: 10.3390/ma16134720

25. Qian H, Lei T, Lei P, Hu Y. Additively manufactured tantalum implants for repairing bone defects: a systematic review. *Tissue Eng B Rev*. 2021;27(2):166-180.
doi: 10.1089/ten.teb.2020.0134

26. Liu B, Ma Z, Li J, *et al*. Experimental study of a 3D printed permanent implantable porous Ta-coated bone plate for fracture fixation. *Bioact Mater*. 2022;10:269-280.
doi: 10.1016/j.bioactmat.2021.09.009

27. Jin J, Wang D, Qian H, *et al*. Precision pore structure optimization of additive manufacturing porous tantalum scaffolds for bone regeneration: a proof-of-concept study. *Biomaterials*. 2025;313:122756.

doi: 10.1016/j.biomaterials.2024.122756

28. Balla VK, Banerjee S, Bose S, Bandyopadhyay A. Direct laser processing of a tantalum coating on titanium for bone replacement structures. *Acta Biomater*. 2010;6(6):2329-2334. doi: 10.1016/j.actbio.2009.11.021

29. Sautet P, Parratte S, Mékidèche T, *et al*. Antibiotic-loaded tantalum may serve as an antimicrobial delivery agent. *Bone Joint J*. 2019;101-B(7):848-851. doi: 10.1302/0301-620X.101B7.BJJ-2018-1206.R1

30. Wang X, Liu W, Jiang C, *et al*. Research progress on the osteogenic properties of tantalum in the field of medical implant materials. *J Mater Res Technol*. 2024;30:1706-1715. doi: 10.1016/j.jmrt.2024.03.200

31. Zhou Z, Liu D. Mesenchymal stem cell-seeded porous tantalum-based biomaterial: a promising choice for promoting bone regeneration. *Colloids Surf B Biointerfaces*. 2022;215:112491. doi: 10.1016/j.colsurfb.2022.112491